ENGINEERING Information Technology & Electronic Engineering
https://www.academax.com/EITEE; https://www.engineering.org.cn
https://ieeexplore.ieee.org/xpl/RecentIssue.jsp?punumber=11344065
E-mail: eng.itee@zju.edu.cn

Research Article
https://doi.org/10.1631/ENG.ITEE.2025.0021

Superresolution reconstruction of E-field for assessing millimeter-wave exposure based on gradient-informed generative adversarial networks with plane-wave integral representation

Shiwei YI[1,2], Congsheng LI[1], Tongning WU[1]✉

[1]*China Academy of Information and Communications Technology, Beijing 100191, China*
[2]*The State Radio Monitoring Center Testing Center, Beijing 100041, China*

Abstract: Accurate assessment of human exposure to millimeter-wave (mmWave) electric fields (E-fields) has recently become critical for public health and safety. High-spatial-resolution E-field distribution is required for assessment of mmWave electromagnetic exposure according to the International Electrotechnical Commission (IEC) and the Institute of Electrical and Electronics Engineers (IEEE) (IEC/IEEE 63195-2 standard). This study proposes a generative adversarial network (GAN) integrated with field gradient loss, termed EFGraGAN, for superresolution reconstruction of mmWave E-fields. The incorporation of E-field gradient loss enables the network to learn both local field magnitudes and spatial structures, thereby enhancing the accuracy and fine structural details of reconstructed E-field maps. To improve generalization across antenna types, the training dataset is generated using plane-wave integral representation (PWIR) and randomized parametric incidence, simulating diverse field distributions. Combined with bilinear interpolation, the method achieves high-resolution reconstruction at 30 GHz and 60 GHz, meeting the requirements of the IEC/IEEE 63195-2 standard for exposure assessment. Numerical simulations show that EFGraGAN reconstructs E-field distributions in a skin phantom with a maximum mean relative error (MRE) of <9% up to 60 GHz in a 4×4 dipole array scenario, outperforming conventional interpolation and traditional GAN methods. The approach also demonstrates strong robustness to noise, enabling current measurement systems to achieve accurate and efficient evaluation of mmWave exposure.

Key words: Field reconstruction; Generative adversarial network (GAN); Millimeter-wave (mmWave) exposure

1 Introduction

With the rapid application of millimeter-wave (mmWave) technology, public concerns regarding the potential adverse health effects of excessive exposure to electromagnetic (EM) fields have increased (Lin, 2016; Yang et al., 2021). Accurate evaluation of mmWave exposure has become an increasingly significant issue. At frequencies >6 GHz, the specific absorption rate (SAR) becomes less relevant for exposure assessment due to the extremely shallow penetration depth of millimeter waves. Instead, the incident power density (IPD) is adopted as the primary compliance metric, particularly for measurement (Wu et al., 2013; IEC/IEEE, 2022a). IPD refers to the power per unit area of EM radiation incident on a surface in free space and can be assessed at distances close to the radiating source. As IPD can be derived from the electric field (E-field) (Wu et al., 2024), measurement systems equipped with either a single probe or probe arrays are commonly used to determine the values at discrete sampling points. In such kinds of systems, the spacing between these sampling points drastically influences the precision of assessment. Denser sampling can reduce the uncertainty in E-field distributions. However, it will introduce pronounced coupling effects (Qamar et al., 2016) and lead to measurement errors. Currently, the minimal spacing of probes has not been standardized, while the interval for the current measurement system is claimed to be around 7–8 mm (Liu et al., 2020). Meanwhile, sampling resolution and spatial gradients are critical for the accurate localization and assessment of the maximum exposure value (IEC/IEEE, 2020, 2022a). Specifically, when assessing mmWave exposure, for evaluating the peak spatial-average IPD, the value is calculated with a step size of 1 mm or $\lambda/10$, whichever is less (IEC/IEEE, 2022a, 2022b). In such a case, there is an urgent need to reconstruct the E-field at much higher resolution, for instance, from the spatial interval of 8 mm to 1 mm (e.g., 10 GHz) and even to 0.5 mm (up to 60 GHz). Traditional interpolation methods often fail to provide sufficient details and accuracy

✉ Tongning WU, wutongning@caict.ac.cn
Shiwei YI, https://orcid.org/0009-0007-1412-1865
Congsheng LI, https://orcid.org/0000-0002-7658-1943
Tongning WU, https://orcid.org/0000-0002-9894-9518
CLC number: TN015

Received: Sept. 7, 2025; Revision accepted: Mar. 26, 2026;
Crosschecked: Apr. 20, 2026; Published online: May 20, 2026

(Wang X et al., 2023), necessitating the development of advanced reconstruction techniques. Otherwise, the current measurement systems, which are of high cost, would become obsolete.

In recent years, generative adversarial networks (GANs) have emerged as a powerful tool for image reconstruction. Conditional GAN (CGAN) introduces conditional information to enable the generator to produce specific types of data on demand (Mirza and Osindero, 2014). Notably, superresolution GAN (SRGAN) (Ledig et al., 2017) uses adversarial training combined with perceptual loss to generate high-resolution images with realistic textures, establishing a benchmark for image SR. This has inspired researchers to explore the application of GANs for SR reconstruction of E-field and magnetic field distributions (Guo LT et al., 2021). However, directly applying generic GAN frameworks to EM field reconstruction presents significant challenges. First, GANs typically require massive training datasets to learn effective feature representations (Lepcha et al., 2023). In EMs, constructing detailed antenna models and performing full-wave simulations are computationally expensive and time-consuming. Furthermore, data derived from specific emitters often lack generalization capability across different antenna geometries. Second, while perception-driven methods improve visual sharpness, they were originally designed based on the statistical properties of natural images. When applied to EM fields, they tend to generate "hallucinated" textures and geometric distortions (Ma et al., 2020; Yan et al., 2024). Unlike natural images, EM field distributions must adhere to physical laws (e.g., Maxwell's equations), in which such artifacts represent nonphysical solutions rather than mere visual flaws. Studies in computer vision suggest that gradient constraints can sharpen details and suppress artifacts (Ma et al., 2020). However, standard frameworks (Ledig et al., 2017) typically rely on the mean-squared error (MSE), perceptual loss, and adversarial loss, neglecting gradient information. Consequently, these methods, while enhancing sharpness, often fail to preserve the continuous variations and strictly defined gradients inherent to E-field distributions, leading to inaccurate field reconstruction.

Aiming to resolve this issue, this study proposes a GAN with a loss function integrating E-field gradient information to refine the SR reconstruction of E-fields (EFGraGAN). The gradient loss learns not only the magnitude of individual scanning points but also the field gradient between adjacent scanning points. The training dataset was generated using plane-wave integral representation (PWIR) (Li CS et al., 2016) and randomized weighted superposition to enhance generalization. EFGraGAN can reconstruct the E-field from 8 mm×8 mm (roughly the spatial interval for the probes in the probe-array system) to 1 mm×1 mm and 0.5 mm×0.5 mm (combined with bilinear interpolation (BI)). The method provides an effective solution for using the current measurement system to evaluate mmWave exposure with improved accuracy and efficiency. The major contributions of this work are as follows.

1. Integrating E-field gradient loss to improve the accuracy of field reconstruction: By incorporating the E-field gradient loss into the GAN framework, the maximum mean relative error (MRE) of the reconstructed E-field distribution is reduced to <9% up to 60 GHz.

2. Leveraging PWIR and randomized weighted superposition to enhance the generalizability of the method: By generating a diversified training dataset covering various incident angles and polarization states using the PWIR and randomized weighted-wave superposition, the dependency on specific antenna structures is reduced, enabling the model to maintain low errors across different antenna types and effectively addressing the issues regarding the generalization of the dataset.

3. Combining EFGraGAN and BI to achieve 16× high-resolution reconstruction: By combining EFGraGAN (8×) with BI (2×), a 16× high-resolution reconstruction (from 8 mm to 0.5 mm) is achieved at 30 GHz and 60 GHz frequencies, meeting the requirements of the International Electrotechnical Commission (IEC) and the Institute of Electrical and Electronics Engineers (IEEE) (IEC/IEEE 63195-2 standard) for the assessment of peak spatial-average IPD (IEC/IEEE, 2022b).

2 Methods and materials

2.1 Architecture of EFGraGAN

EFGraGAN comprises a generator (G) and a discriminator (D) network, as shown in Fig. 1.

The generator (G) generates a higher-resolution E-field (E_{GHR}) based on the low-resolution E-field (E_{LR}). G consists of 15 identical residual blocks, where each block includes two 3×3 convolutional layers with 64 feature maps, followed by batch normalization and a parametric rectified linear unit (PReLU) activation function. Then, three PixelShuffle layers are used to enhance the output resolution by a factor of 8.

The discriminator (D) evaluates the authenticity of the input e-field (e.g., E_{GHR}). If D incorrectly classifies the input E-field as a simulated high-resolution E-field (E_{SHR}), it indicates that G has not yet fully learned the true distribution characteristics of the E-field. D consists of seven convolutional layers with the dimension of feature

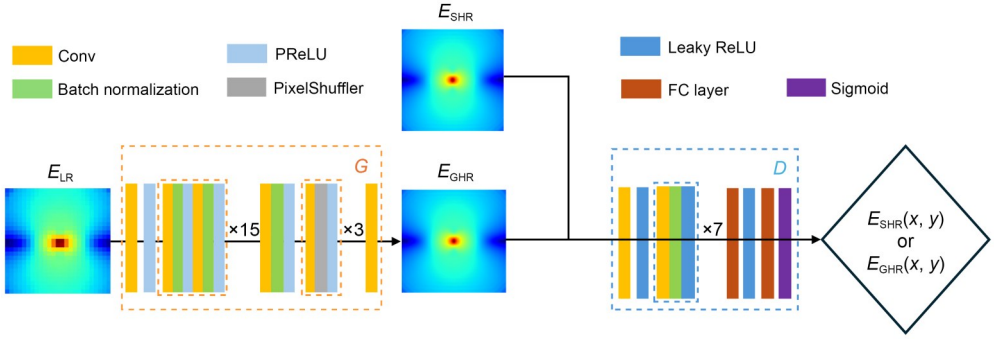

Fig. 1 Framework of EFGraGAN

maps increasing from 64 to 512, each followed by batch normalization and a leaky ReLU activation function (α=0.2). Following these are two fully connected (FC) layers, where the first FC layer maps the 512-dimensional vector to a 1024-neuron layer with leaky ReLU activation, and the second FC layer further reduces the 1024-dimensional vector to a one-dimensional (1D) scalar output. Then, D outputs a probability value within the [0, 1] range through the sigmoid function, determining whether the input E-field is real or generated.

Furthermore, G optimizes its parameters to produce an instance of E_{GHR} that closely matches the statistical characteristics of E_{SHR}. This process aims to convince the network D that the obtained E_{GHR} fields are indistinguishable from E_{SHR} by minimizing the total loss through their iterative competition. The loss function L consists of four parts as follows:

$$L = L_{\mathrm{mse}} + \alpha L_{\mathrm{per}} + \beta L_{\mathrm{adv}} + \gamma L_{\mathrm{grad}}\,, \tag{1}$$

where α, β, and γ are the weights assigned to the perceptual, adversarial, and gradient losses, respectively. α=0.005, β=0.005, and γ=0.01 are optimized according to a previous study (Ma et al., 2020). L_{grad} is the proposed gradient loss of the E-field amplitude. Adopting a relatively large γ value enables the network to place greater emphasis on gradient domain constraints, which helps generate sharp edges with almost no artifacts (Sun et al., 2011).

The first three parts of the loss are defined as

$$L_{\mathrm{mse}}=\frac{1}{N}\sum_{i=1}^{N}\left(E_{\mathrm{GHR}}(x_i,y_i)-E_{\mathrm{SHR}}(x_i,y_i)\right)^2, \tag{2}$$

$$L_{\mathrm{per}}=\frac{1}{M}\frac{1}{N}\sum_{m=1}^{M}\sum_{i=1}^{N}\left(F_m\left(E_{\mathrm{GHR}}(x_i,y_i)\right)-F_m\left(E_{\mathrm{SHR}}(x_i,y_i)\right)\right)^2, \tag{3}$$

$$L_{\mathrm{adv}}=-\frac{1}{N}\sum_{i=1}^{N}\left(\log\left(D\left(E_{\mathrm{SHR}}(x_i,y_i)\right)\right)+\log\left(1-D\left(G\left(E_{\mathrm{LR}}(x_i,y_i)\right)\right)\right)\right), \tag{4}$$

where (x_i, y_i) represents the location of the E-field and i=1, 2, ⋯, N denotes the index of each data point. F_m denotes the feature mapping function of the m^{th} (m=1, 2, ⋯, M, where M denotes the number of feature layers) layer of a pretrained feature extraction network (VGG19).

The gradient of the mmWave E-field intensity reveals the spatial characteristics of the field strength distribution, in addition to being correlated with the local power absorption and the peak location of IPD. Thus, the E-field gradient is incorporated as a key physical constraint into the reconstruction process, ensuring that the reconstructed field preserves the spatial differential structure. The proposed E-field amplitude gradient loss can be defined as

$$\begin{aligned}L_{\mathrm{grad}}=&\frac{1}{N}\sum_{i=1}^{N}\left(\frac{E_{\mathrm{SHR}}(x_i+h,y_i)-E_{\mathrm{SHR}}(x_i-h,y_i)}{2h}\right.\\&\left.-\frac{E_{\mathrm{GHR}}(x_i+h,y_i)-E_{\mathrm{GHR}}(x_i-h,y_i)}{2h}\right)^2\\&+\frac{1}{N}\sum_{i=1}^{N}\left(\frac{E_{\mathrm{SHR}}(x_i,y_i+h)-E_{\mathrm{SHR}}(x_i,y_i-h)}{2h}\right.\\&\left.-\frac{E_{\mathrm{GHR}}(x_i,y_i+h)-E_{\mathrm{GHR}}(x_i,y_i-h)}{2h}\right)^2,\end{aligned} \tag{5}$$

where h represents the spatial resolution of the high-resolution E-field.

2.2 Generation of datasets for network training

The network is designed to reconstruct the high-resolution e-field from its low-resolution counterpart. To train the model, paired datasets containing both high-resolution and the corresponding low-resolution E-field values need to be generated. The dataset's representation is enhanced through two approaches, namely, increasing the variability in E-field spatial distributions by PWIR and diversifying the configurations of exposure patterns by randomized weighted-wave superposition. The process of constructing each $E_{\mathrm{SHR}}(x,y)$ is shown in Fig. 2.

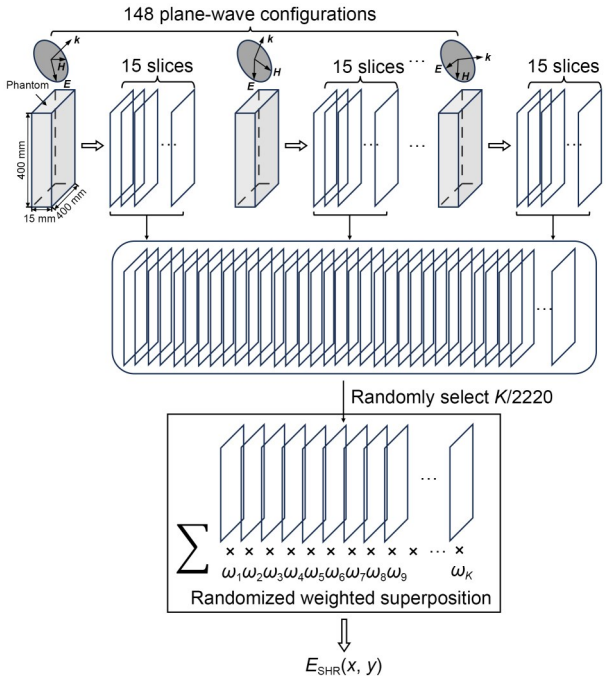

Fig. 2 Generation of $E_{\mathrm{SHR}}(x,y)$ for model training

2.2.1 Generating datasets using PWIR

In this study, PWIR (Li CS et al., 2016) with numerical simulation was used to generate the E-field slice dataset as follows:

$$\boldsymbol{E}(\boldsymbol{r}) = \sum_{l=1}^{K} A_l \exp\left(\mathrm{j}\boldsymbol{k}_l \cdot \boldsymbol{r} + \phi_l\right)\boldsymbol{v}_l\,, \tag{6}$$

where $\boldsymbol{r}$ represents the spatial position vector, K is the number of plane waves, and A_l, $\boldsymbol{k}_l$, ϕ_l, and $\boldsymbol{v}_l$ represent the amplitude, propagation direction, phase, and polarization of the l^{th} plane wave, respectively.

A skin phantom with dimensions of 400 mm×400 mm×15 mm was used in the numerical simulation (IEC/IEEE, 2020). The frequency-dependent conductivity and relative permittivity of the phantom were adopted from Li K et al. (2024).

The simulation configuration for generating the training dataset is described in Fig. 3. We sampled θ from 0° to 180° with an interval of 5° and ψ from 0° to 360° with an interval of 90°, and φ was fixed at 90°. It yielded a total of 37×4=148 plane-wave configurations.

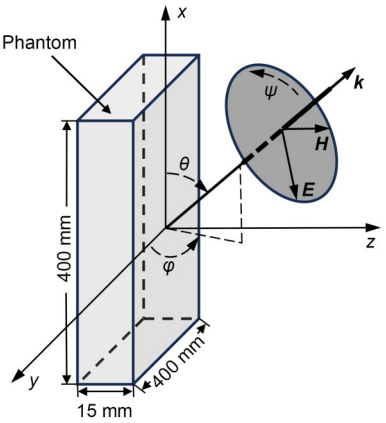

Fig. 3 Configuration of plane wave for simulation. *E* represents the E-field, *H* represents the magnetic field, *k* represents the propagation direction, *θ* and *φ* represent the propagation angles, and *ψ* represents the polarization angle

This configuration has been demonstrated to effectively represent random reflected waves in the reverberation chamber (Wu et al., 2010; Li CS et al., 2016). The plane-wave amplitude and phase of the wave were maintained at 1 and 0, respectively.

Consequently, finite-difference time-domain (FDTD) simulations were performed using the SEMCAD-X v14.8 platform (SPEAG AG, Zurich, Switzerland) with uniform cubic voxels of 1 mm^3 (10 GHz) and 0.5 mm^3 (30 and 60 GHz). The minimum distance between the absorption boundary (10-layer perfectly matched layer (PML)) and the phantom was 40 mm.

The E-field in the phantom was computed and sliced at 1 mm intervals along the *z*-axis, resulting in a total of 148 (number of configurations)×15 (number of slices)=2220 E-field slices $\{\boldsymbol{E}_n(x,y)\}$, where n =1, 2, ⋯, 2220 for the E-field slice dataset.

2.2.2 Data augmentation using randomized weighted-wave superposition

K incident waves ($\{\boldsymbol{E}_t(x,y)\}$, t =1, 2, ⋯, K) were randomly selected from $\{\boldsymbol{E}_n(x,y)\}$. Each selected $\{\boldsymbol{E}_t(x,y)\}$ was assigned a complex weight w_t, where $w_t=a_t e^{j\beta_t}$, $a_t\in[0,1]$, $\beta_t\in[0,2\pi)$. $\boldsymbol{E}_{\mathrm{SR}}(x,y)$ was obtained through weighted superposition of the K incident waves according to $\boldsymbol{E}_{\mathrm{SR}}(x,y)=\sum_{t=1}^{K}\omega_t\boldsymbol{E}_t(x,y)$. This process, as illustrated in Fig. 2, was repeated 8000 times to generate 8000 data samples (E-field distribution on the slices), in which the magnitude values $E_{\mathrm{SHR}}(x,y)$ formed the complete dataset. The data were then downsampled by a factor of 8 for 10 GHz and by 16 for 30 GHz and 60 GHz, respectively, resulting in low-resolution datasets $E_{\mathrm{LR}}(x,y)$. $E_{\mathrm{LR}}(x,y)$ were inputted into the G network. The batch size and number of training epochs were 16 and 300, respectively. We set the learning rate to 0.0001 for both G and D, and then reduced it by half at 50 000 and 100 000 iterations. The strategy of learning rate decay helps the model converge better during the training process. For optimization, we used adaptive moment estimation (Adam) with β_1=0.9 and β_2=0.999. The above numerical setup ensures comparability and fairness of the simulations.

2.3 Numerical validation

Numerical validation used full-wave simulations at 10 GHz (with a spatial resolution of 1 mm×1 mm×1 mm), 30 GHz, and 60 GHz (with a spatial resolution of 0.5 mm×0.5 mm×0.5 mm) for exposure assessments using a single dipole antenna, a 4×4 dipole array, and a pyramidal horn antenna. Fig. 4 illustrates the three antennas used for validation.

The dimensions of the single dipole antenna and the dipole array were adapted from Li K et al. (2024). The dipole exposure sources were positioned 5 mm above the center of the phantom. The spacing between adjacent dipoles in the dipole array was set to $\lambda/2$ (half wavelength). The total input power (for both the single dipole antenna and the 4×4 dipole array) was set to 10 mW (Li K et al., 2023).

The dimensions of the pyramidal horn antenna were adapted from previous publications (IEC/IEEE, 2022a). The exposure sources were positioned at distances of 2, 5, 10, and 50 mm to the surface of the phantom. The net input power was set to 10 mW. The dimensions for the pyramidal horn antenna are shown in Table 1.

We selected MRE, structural similarity index measure (SSIM), and gradient magnitude similarity deviation (GMSD) as evaluation metrics. MRE is defined as

$$\mathrm{MRE}=\frac{1}{N}\sum_{i=1}^{N}\frac{\left|E_{\mathrm{GHR}}(x_i,y_i)-E_{\mathrm{SHR}}(x_i,y_i)\right|}{E_{\mathrm{SHR}}(x_i,y_i)}\times 100\%, \tag{7}$$

where $E_{\mathrm{SHR}}(x_i,y_i)$ is the i^{th} E-field calculated by the numerical solver with a resolution of 0.5 mm, and $E_{\mathrm{GHR}}(x_i,y_i)$ is the i^{th} E-field generated by the proposed network.

MRE provides a direct measurement of error percentage at each point, making it particularly suitable for assessing numerical accuracy. Compared to MSE or mean absolute error (MAE), MRE prevents error-masking caused by variations in field strength magnitude.

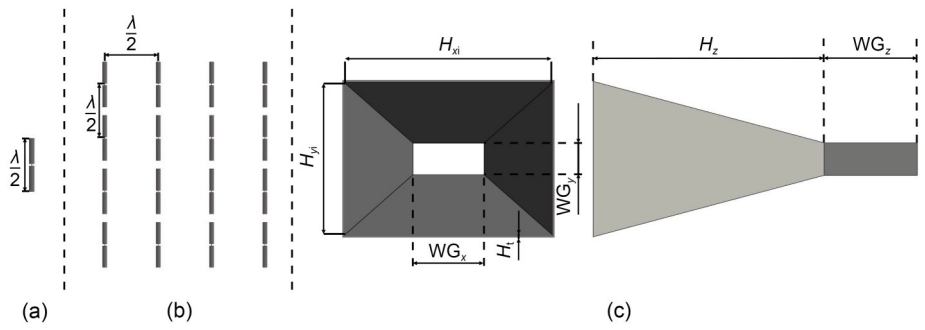

Fig. 4 A single dipole antenna (a), a 4×4 dipole array (b), and a pyramidal horn antenna (c), where the front view is on the left, and the side view is on the right

Table 1 Dimensions for the pyramidal horn antenna at each frequency

f (GHz)	H_{xi} (mm)	H_{yi} (mm)	H_z (mm)	H_t (mm)	WG_x (mm)	WG_y (mm)	WG_z (mm)
10	67.6	49.5	108.0	1.5	22.9	10.2	30.0
30	40.8	31.7	47.2	1.3	7.1	3.6	11.0
60	21.3	16.7	24.8	1.3	3.8	1.9	6.2

H and WG denote the dimensions of the flared horn section and the feeding waveguide, respectively. The subscripts *x*, *y*, and *z* indicate the dimensions along the corresponding Cartesian axes, and the subscript i denotes the internal cavity dimensions of the horn aperture. H_t represents the wall thickness, and *f* represents the frequency

To evaluate the similarity of the E-field distributions, the SSIM metric was used. As shown in Eq. (8), it assesses the structural similarity through three comparative dimensions: luminance based on mean intensity, contrast derived from variance, and structure determined by covariance.

$$\mathrm{SSIM}=\frac{\left(2\mu_X\mu_Y+C_1\right)\left(2\sigma_{XY}+C_2\right)}{\left(\mu_X^2+\mu_Y^2+C_1\right)\left(\sigma_X^2+\sigma_Y^2+C_2\right)}, \tag{8}$$

where μ_X and μ_Y are the mean values of $E_{\mathrm{SHR}}(x_i,y_i)$ and $E_{\mathrm{GHR}}(x_i,y_i)$, respectively, σ_X and σ_Y are the standard deviations of $E_{\mathrm{SHR}}(x_i,y_i)$ and $E_{\mathrm{GHR}}(x_i,y_i)$, respectively, and σ_{XY} denotes the covariance of $E_{\mathrm{SHR}}(x_i,y_i)$ and $E_{\mathrm{GHR}}(x_i,y_i)$. C_1 and C_2 are 0.01 and 0.03, respectively (Wang Z et al., 2004).

MRE and SSIM provide complementary measures of reconstruction quality, with MRE quantifying numerical precision and SSIM assessing structural fidelity.

In addition, GMSD was adopted to quantify textures and blur reduction by analyzing local gradient variations (Xue et al., 2014). It quantifies distortion by computing the local similarity of gradient magnitudes, making it highly sensitive to blur, noise, and texture degradation.

Convolving the Prewitt filters h_x and h_y with the reference and the generated E-fields yields the horizontal and vertical gradient images of E_{SHR} and E_{GHR}. The gradient magnitudes of E_{SHR} and E_{GHR} at location (x_i,y_i), denoted by $m_{\mathrm{SHR}}(x_i,y_i)$ and $m_{\mathrm{GHR}}(x_i,y_i)$, are computed as

$$m_{\mathrm{SHR}}(x_i,y_i)=\sqrt{\left(E_{\mathrm{SHR}}\otimes h_x\right)^2(x_i,y_i)+\left(E_{\mathrm{SHR}}\otimes h_y\right)^2(x_i,y_i)}, \tag{9}$$

$$m_{\mathrm{GHR}}(x_i,y_i)=\sqrt{\left(E_{\mathrm{GHR}}\otimes h_x\right)^2(x_i,y_i)+\left(E_{\mathrm{GHR}}\otimes h_y\right)^2(x_i,y_i)}, \tag{10}$$

where the symbol "⊗" denotes the convolution operation.

With the gradient magnitude maps m_{SHR} and m_{GHR} in hand, the gradient magnitude similarity (GMS) map is computed as

$$\mathrm{GMS}(x_i,y_i)=\frac{2m_{\mathrm{SHR}}(x_i,y_i)m_{\mathrm{GHR}}(x_i,y_i)+c}{m_{\mathrm{SHR}}^2(x_i,y_i)+m_{\mathrm{GHR}}^2(x_i,y_i)+c}, \tag{11}$$

where c is a positive constant that supplies numerical stability and c=0.0026 (Xue et al., 2014). GMSD is represented as

$$\mathrm{GMSD}=\sqrt{\frac{1}{N}\sum_{i=1}^{N}\left(\mathrm{GMS}(x_i,y_i)-\mu_{\mathrm{GMS}}\right)^2}, \tag{12}$$

where μ_{GMS} is the mean of the GMS values.

Note that the value of GMSD reflects the range of distortion severities in an image. The higher the GMSD score, the larger the distortion range and the lower the perceptual quality of the image.

2.4 Hardware configuration

All computations were executed on a workstation with dual Intel Xeon Gold 6230 central processing units (CPUs) (40 cores and 80 threads), 64 GB random access memory (RAM), and dual NVIDIA Quadro P5000 graphics processing units (GPUs) (NVIDIA, Santa Clara, CA, USA, 32 GB memory on board), leveraging compute unified device architecture (CUDA)-based parallel computing and multicore CPU processing to optimize the overall computational time.

3 Results and discussion

In this study, the proposed method is numerically investigated considering three aspects: field reconstruction performance using different types of antennas, noise sensitivity, and computational time. To note, as the GAN-based networks SRGAN and EFGraGAN do not converge for 16× SR reconstruction (from 8 mm to 0.5 mm) for 30 GHz and 60 GHz, we use 8× EFGraGAN to reconstruct the field from 8 mm to 1 mm, followed by a 2× BI for 1 mm to 0.5 mm.

3.1 Trade-off analysis for selection of the incident wave number

We reference the plane-wave configuration of Wu et al. (2010), who demonstrated that using >100 incident plane waves achieves stable EM exposure assessments; they used 200 plane waves in their simulations. To further determine the number of incident waves, we conduct a series of preliminary simulations, evaluating the performance of various incident-wave combinations (e.g., K=100, 150, 200, 250, and 300) within the incident field configuration parameters ($\theta\in[0°, 180°]$ and $\psi\in[0, 2\pi)$). Table 2 presents the modeling accuracy (quantified by MRE) and computational time for the 60-GHz 4×4 dipole array scenario.

Table 2 Quantitative trade-off between reconstruction accuracy (MRE) and computational time for various incident-wave combinations (*K*)

K	MRE (%)	Time (s)
100	10.74	2500
150	9.12	5200
200	8.75	7844
250	8.75	14 000
300	8.74	25 000

We observe that accuracy initially increases rapidly with the number of incident waves, but eventually saturates, while computational time grows exponentially. Specifically, a comprehensive trade-off analysis reveals that when the number of incident waves reaches 200, the accuracy reaches 8.75%; further increasing the number results in only marginal improvements in accuracy but incurs a

significant increase in computational time. Therefore, a combination of 200 incident waves achieves an optimal balance between high accuracy and computational efficiency.

3.2 Field reconstruction using different types of antennas

Table 3 presents the reconstruction results on the phantom surface of the single dipole antenna, the 4×4 dipole array, and the pyramidal horn antenna at different frequencies. The reconstruction performance decreases marginally as the complexity of the antenna rises. For EFGraGAN, although the maximum MRE of the 4×4 dipole array reaches 8.75%, it still meets the requirements of the standard (<10% as indicated by IEC/IEEE (2022b)). At the same frequency, EFGraGAN performs the best among all methods in terms of MRE, SSIM, and GMSD.

Fig. 5 shows the reconstructed E-field distributions on the phantom surface under exposure from a single dipole antenna, a 4×4 dipole array, and a pyramidal horn antenna. It can be observed that the proposed method suppresses artifacts and sharpens the details compared to other methods.

3.3 Field reconstruction of pyramidal horn antennas at different distances to the phantom surface

Table 4 presents the reconstructed E-field distributions on the phantom surface under exposure to pyramidal horn antennas at varying distances. In accordance with the antenna-to-surface distance configurations specified by IEC/IEEE (2022a) for system validation, the results demonstrate that reconstruction accuracy is improved with increasing distance between the antenna and the phantom surface.

The reconstructed E-fields obtained using EFGraGAN (and BI) exhibit fewer blurred regions and clearer edge structures, as shown in Fig. 6.

All results indicate that MRE increases with frequency for all methods, which suggests that higher frequencies present greater reconstruction challenges. Compared with other methods, the increased rate of MRE for EFGraGAN is the lowest. The improvement in SSIM and reduction in GMSD jointly indicate that gradient constraints are effective in preserving structural information for high-resolution reconstruction of E-field distributions. As can also be observed from Figs. 5 and 6, the proposed method mitigates artifacts and is clearly more effective than the other methods for E-field reconstruction.

3.4 Quantitative validation through 1D line profiles across peak E-field regions

Fig. 7 shows the 1D line profiles extracted through peak E-field regions, which are used to validate the results in Figs. 5 and 6.

Table 3 Comparison of reconstructed E-fields on the phantom surface for the single dipole antenna, the 4×4 dipole array, and the pyramidal horn antenna at different frequencies

Antenna type	f (GHz)	MRE (%)				SSIM				GMSD			
		BI	CI	SRGAN	EFGraGAN	BI	CI	SRGAN	EFGraGAN	BI	CI	SRGAN	EFGraGAN
Single dipole antenna	10	7.98	7.80	5.38	3.67	0.86	0.85	0.93	0.95	0.11	0.11	0.08	0.07
	30	20.24	19.88	9.98*	5.89*	0.88	0.86	0.90*	0.92*	0.14	0.14	0.10*	0.09*
	60	37.64	37.82	15.64*	7.49*	0.89	0.87	0.86*	0.91*	0.15	0.17	0.12*	0.10*
4×4 dipole array	10	18.90	18.29	6.47	3.82	0.83	0.82	0.90	0.93	0.13	0.11	0.10	0.08
	30	43.76	42.28	12.12*	6.44*	0.80	0.79	0.86*	0.91*	0.16	0.15	0.13*	0.11*
	60	68.96	68.78	18.86*	8.75*	0.72	0.71	0.80*	0.88*	0.20	0.19	0.17*	0.11*
Pyramidal horn antenna	10	11.20	10.95	5.72	3.76	0.90	0.90	0.92	0.95	0.13	0.12	0.09	0.08
	30	21.30	20.90	10.12*	6.35*	0.89	0.89	0.88*	0.91*	0.15	0.14	0.12*	0.10*
	60	38.50	38.10	17.45*	7.82*	0.72	0.71	0.81*	0.89*	0.17	0.17	0.16*	0.11*

* This result is jointly generated by SRGAN/EFGraGAN (8×) and BI (2×). CI: cubic interpolation

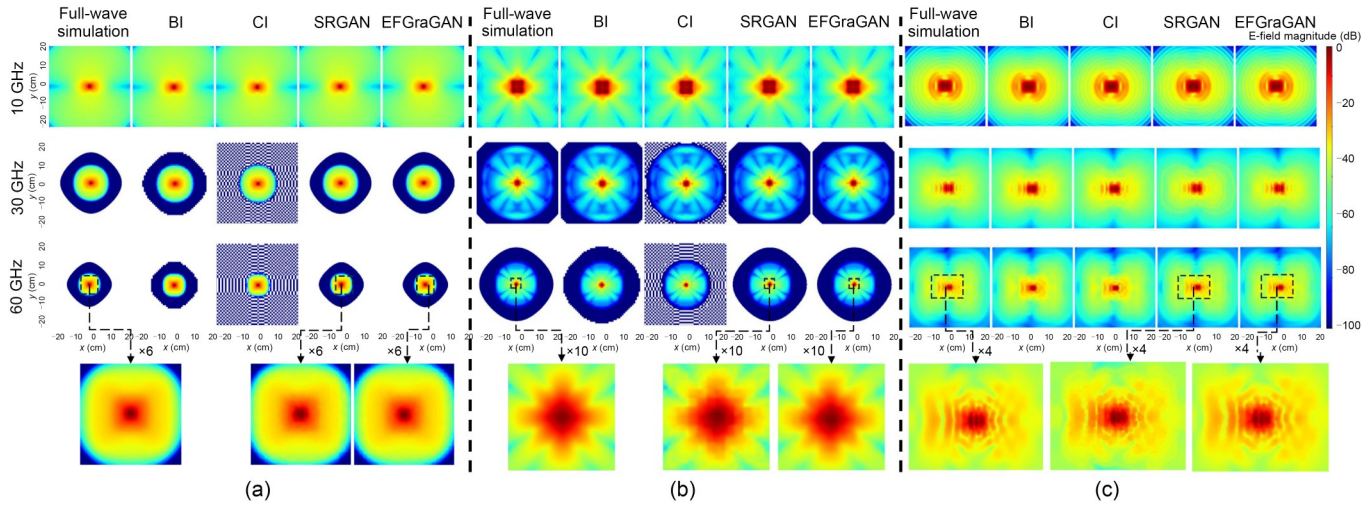

Fig. 5 Comparison of reconstructed E-field distributions on the phantom surface at a 5 mm distance from the antenna: (a) single dipole antenna; (b) 4×4 dipole array; (c) pyramidal horn antenna. The E-field magnitude is referenced to 10 V/m

Table 4 Comparison of reconstructed E-fields on the phantom surface for pyramidal horn antennas at varying frequencies and distances

f (GHz)	Distance (mm)	MRE (%)				SSIM				GMSD			
		BI	CI	SRGAN	EFGraGAN	BI	CI	SRGAN	EFGraGAN	BI	CI	SRGAN	EFGraGAN
10	2	14.80	14.52	6.85	4.23	0.81	0.80	0.89	0.92	0.15	0.14	0.12	0.10
	5	11.20	10.95	5.72	3.76	0.83	0.82	0.90	0.93	0.13	0.11	0.10	0.08
	10	8.50	8.32	4.98	3.45	0.85	0.84	0.91	0.95	0.11	0.10	0.09	0.08
	50	6.20	6.05	4.35	3.12	0.90	0.89	0.95	0.96	0.09	0.09	0.08	0.07
30	2	26.50	26.10	12.35*	7.68*	0.78	0.77	0.85*	0.90*	0.18	0.17	0.14*	0.11*
	5	21.30	20.90	10.12*	6.35*	0.80	0.79	0.86*	0.91*	0.16	0.15	0.13*	0.11*
	10	17.80	17.50	8.65*	5.21*	0.82	0.81	0.87*	0.92*	0.15	0.15	0.12*	0.09*
	50	10.20	9.95	5.32*	4.56*	0.88	0.87	0.92*	0.94*	0.10	0.10	0.09*	0.08*
60	2	43.20	42.80	25.60*	8.95*	0.70	0.69	0.78*	0.87*	0.22	0.21	0.18*	0.13*
	5	38.50	38.10	17.45*	7.82*	0.72	0.71	0.80*	0.88*	0.20	0.19	0.17*	0.11*
	10	32.60	32.20	17.80*	6.95*	0.75	0.74	0.82*	0.89*	0.18	0.18	0.16*	0.10*
	50	20.30	19.90	10.25*	5.32*	0.82	0.81	0.86*	0.91*	0.14	0.13	0.12*	0.09*

* This result is jointly generated by SRGAN/EFGraGAN (8×) and BI (2×)

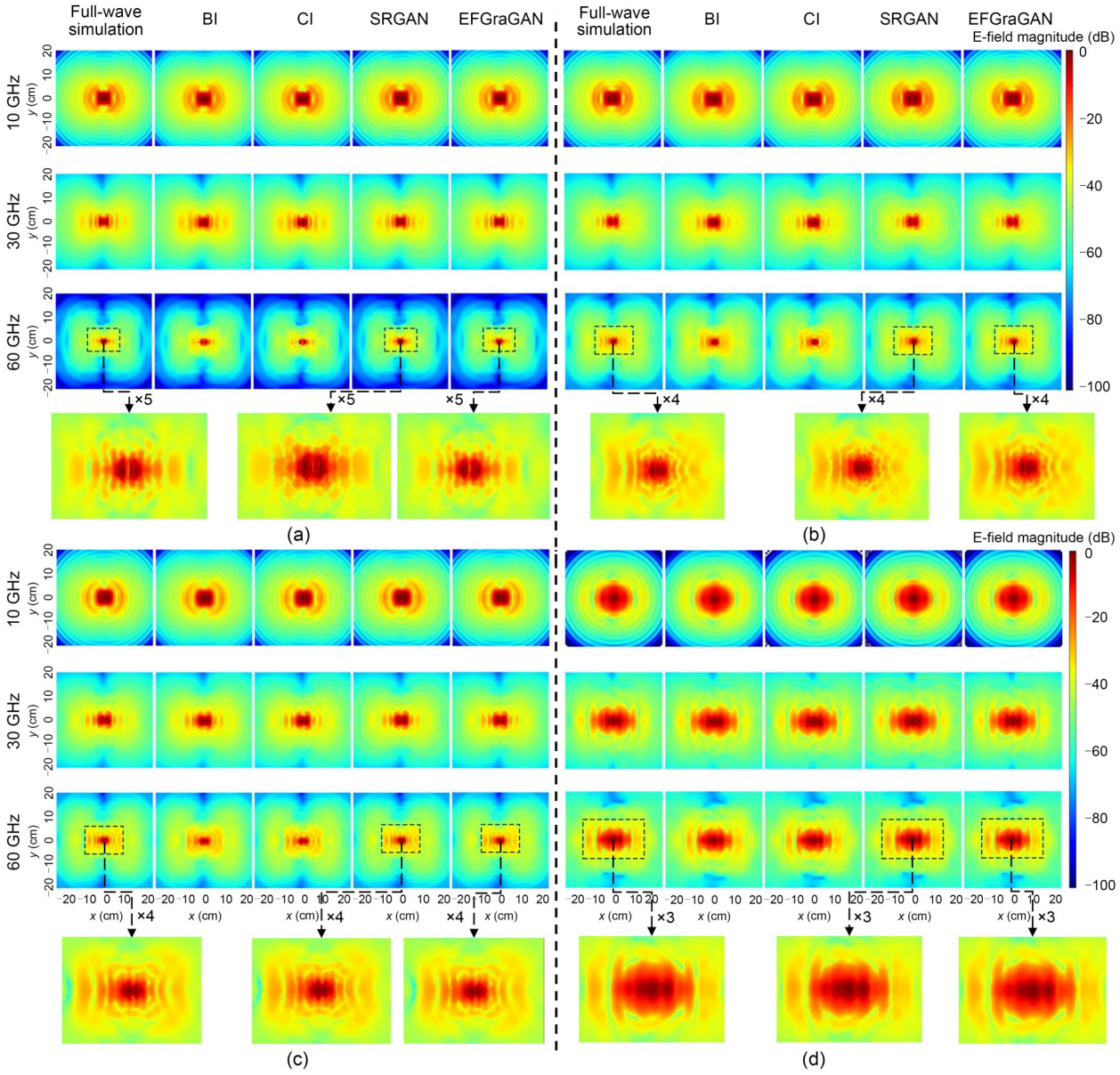

Fig. 6 Comparison of reconstructed E-field distributions on the phantom surface by exposure of pyramidal horn antennas at different distances: (a) 2 mm; (b) 5 mm; (c) 10 mm; (d) 50 mm. The E-field magnitude is referenced to 10 V/m

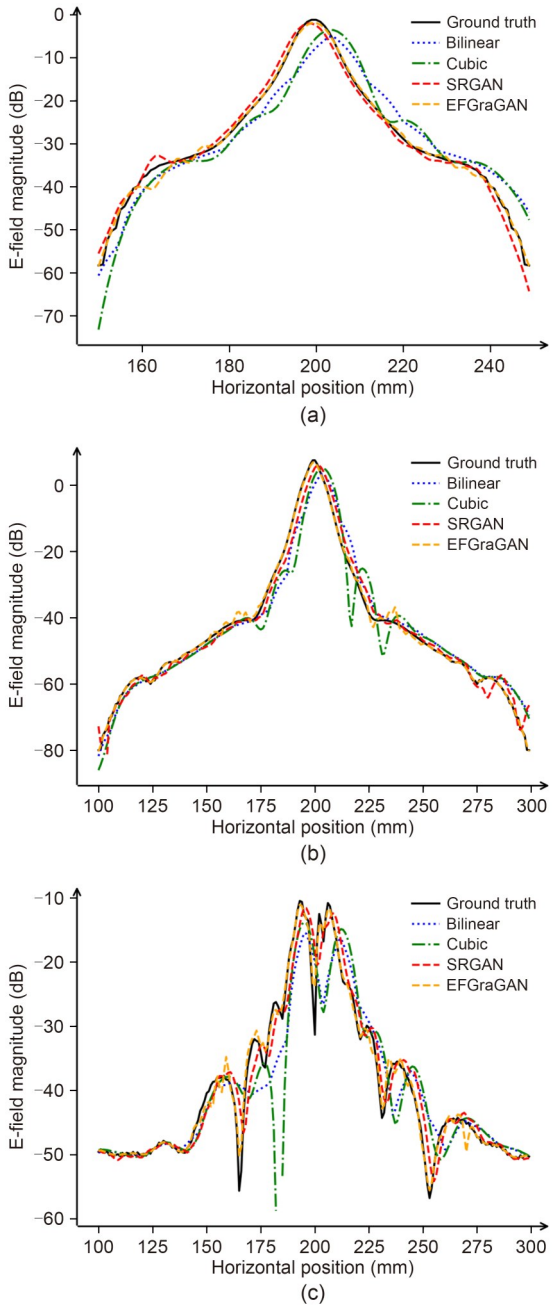

Fig. 7 Quantitative comparison of 1D E-field intensity profiles across peak regions for three representative scenarios, all operating at 60 GHz: (a) a single dipole antenna located at 5 mm above the phantom surface; (b) a 4×4 dipole array positioned at 5 mm above the phantom surface; (c) a pyramidal horn antenna placed at 2 mm above the phantom surface. The E-field magnitude is referenced to 10 V/m

The 1D line profiles demonstrate that our method accurately captures both the location and the magnitude of the field peaks compared to SRGAN and conventional interpolation approaches. Notably, the peak positions predicted by our model are consistent with the ground truth, and the other regions also show better alignment, highlighting the critical role of the gradient constraint in capturing field peaks and sharp boundaries.

3.5 Sensitivity to noise

The reconstruction method is expected to be robust to noise. In such a case, the zero-mean additive white Gaussian noise with different signal-to-noise ratios (SNRs) has been added to low-resolution input data. Table 5 shows the results for the 4×4 dipole array, which has the most significant errors. The results reveal that the MRE of EFGraGAN changes insignificantly, demonstrating its robustness against the additive noise.

Table 5 MRE values of EFGraGAN under different SNR conditions

Antenna type	f (GHz)	MRE (%)			
		EFGraGAN	EFGraGAN (20 dB)	EFGraGAN (30 dB)	EFGraGAN (40 dB)
4×4 dipole array	10 (8×)	3.82	4.25	4.11	3.96
	30 (16×)	6.44	7.25	6.95	6.69
	60 (16×)	8.75	9.56	9.49	8.97

3.6 Comparison of computational time

Table 6 outlines the time cost for EFGraGAN training and inference. The time elapsed for both dataset generation and network training increases with frequency, while the inference time remains constant at 0.38 s, using the present hardware. Our method's inference time is longer than that of BI (0.007 s) and cubic interpolation (CI) (0.016 s) but shorter than that of SRGAN (0.40 s). Although the discriminator and the incorporated gradient loss increase the training complexity, these components are excluded during inference, where only the generator performs a forward propagation to ensure rapid execution.

Table 6 Time cost for EFGraGAN training and inference

f (GHz)	Time cost by EFGraGAN (s)		
	Training		Inference
	Dataset generation	Network training	
10 (8×)	1480	7860	0.38
30 (16×)	7844	7680	
60 (16×)	28416	8100	

Compared with the E-field measurement system with a single probe, measuring the E-field over a surface of 2 cm×2 cm with intervals of 8, 1, and 0.5 mm may cost 27, 1200, and 4800 s, respectively (including 2 s for motion of the robotic arm and 1 s for gauging E-field strength per measurement). Integrating sparse sampling with the proposed SR reconstruction significantly saves time across the entire assessment workflow. This approach is particularly beneficial for repetitive measurement, although the proposed model requires 2.6–10 h for dataset generation and network training, as the network does not require retraining for different antenna types.

The system based on a probe array can measure the E-field within seconds but with coarse sampling intervals. Therefore, the comparison is inapplicable with a system of this type. Notably, the present method can be implemented with the system to enhance its postprocessing accuracy.

3.7 Computational complexity and resource consumption

Table 7 shows the performance comparison across BI, CI, SRGAN, and EFGraGAN, including the number of model parameters, per-frame floating-point operations (FLOPs), per-frame CPU and GPU time, and training-phase GPU memory usage.

Table 7 Comparison of computational complexity and resource consumption across various SR methods

Metric	Value			
	BI	CI	SRGAN	EFGraGAN
Number of parameters (M)	0	0	15.4	16.2
FLOPs per frame (G)	0.02	0.03	29.7	31.5
CPU time (s)	0.007	0.016	<0.02	<0.02
GPU time (s)			0.40	0.38
GPU memory usage (GB)			10.8	11.3

Here, 0.38 s represents the unoptimized end-to-end latency in a standard PyTorch environment, which includes data loading, peripheral component interconnect express (PCIe) tensor transfer, and eager-mode execution overhead. The pure kernel computational time is significantly lower. Traditional interpolation methods are executed entirely on the CPU and do not involve a training phase

As shown in Table 7, the inference time for EFGraGAN is predominantly the GPU time dedicated to parallel tensor operations, whereas the CPU time required for data loading is practically negligible (<0.02 s per frame). Furthermore, the 11.3 GB memory usage refers specifically to the training phase; this memory requirement is drastically reduced during the inference stage.

Conventional interpolation methods feature low computational complexity and resource consumption, but their reconstruction accuracy (MRE of up to 68.96%) cannot satisfy the standards for mmWave exposure assessment, as shown in Table 3. Compared with SRGAN, EFGraGAN achieves a significant improvement in reconstruction accuracy but with slight increase in resource usage: a 5.2% rise in the number of parameters, a 6.1% increase in inference FLOPs, and a 4.6% growth in training GPU memory usage, as shown in Tables 3 and 7. Specifically, for the scenario of the 60-GHz 4×4 dipole array, EFGraGAN reduces the reconstructed MRE from 18.86% to 8.75%, which satisfies the requirements specified in the IEC/IEEE 63195-2 standard (MRE<10%). Therefore, the increase in computational complexity and resource consumption introduced by EFGraGAN is reasonable and acceptable.

3.8 Generalization of the proposed method

At the stage of dataset preparation, three-dimensional (3D) full-wave simulation was used to replicate the propagation characteristics of real EM fields. Meanwhile, the PWIR algorithm was used to simulate the emission mode of mmWave antennas using plane-wave superposition. This approach thus achieves the decoupling of source data and antenna types.

During the numerical validation phase, we conduct numerical evaluations using three commonly used antenna types, demonstrating the model's robustness across different antenna architectures, as shown in Table 3. Additionally, the robustness to noise of the model is assessed by introducing additive white Gaussian noise at SNR levels of 20, 30, and 40 dB to simulate measurement uncertainty, as observed in Table 5. Even under the most challenging condition—a 60-GHz 4×4 dipole array—the error increases only marginally from 8.75% to 9.56%.

These approaches collectively show the enhanced model generalization capacity and ensure its compliance with the spatial resolution and accuracy requirements of the IEC/IEEE 63195-2 standard.

3.9 Future work

This paper proposes EFGraGAN, a GAN-based method that efficiently and accurately reconstructs mmWave E-field distributions. However, similar to most GAN-based approaches, it exhibits training complexity, which leads to prolonged convergence time (Sharma et al., 2024).

Recent advances in physics-informed neural networks (PINNs) have demonstrated their versatility across domains (Chen et al., 2025a, 2025b; Guo MH et al., 2025). The introduction of PINNs enhances the efficiency of data modeling and the stability of network training (Su et al., 2024; Yin et al., 2025). These PINN-based approaches may further improve the stability and convergence of GAN training. We will explore these models in future work.

Additionally, we will conduct further numerical validation when suitable commercial equipment becomes available.

4 Conclusions

This study proposes EFGraGAN, a GAN-based method integrating gradient loss for mmWave E-field SR reconstruction. Using PWIR and randomized weighted superposition for dataset generation, it reduces the dependence on specific antenna structures. Combined with BI, the proposed method achieves 16× high-resolution reconstruction at 30 GHz and 60 GHz, meeting the requirement by exposure assessment standards. The simulations show that EFGraGAN outperforms traditional GANs in terms of MRE, SSIM, and GMSD across various antenna types and distances. It exhibits strong robustness to noise as well. The method balances accuracy and efficiency, saving measurement time significantly, thus providing a reliable tool for evaluating mmWave exposure. Current measurement systems could benefit from this method to cover higher frequency bands.

Acknowledgments

This work was supported by the National Natural Science Foundation of China (No. 62271508) and the Beijing Municipal Foundation of Natural Sciences–Xiaomi Innovation Joint Foundation (No. L233018).

Author contributions

Congsheng LI designed the research. Shiwei YI processed the data and drafted the paper. Tongning WU and Congsheng LI helped organize the paper. Shiwei YI and Tongning WU revised and finalized the paper.

Conflict of interest

All the authors declare that they have no conflict of interest.

Data availability

The data that support the findings of this study are available from the corresponding author upon reasonable request.

Declaration on the use of generative AI tools

During the preparation of this work, the authors used ChatGPT to improve language. After using this tool, the authors reviewed and edited the content as needed and take full responsibility for the content of the published article.

References

Chen Y, Lü X, Jia XJ, et al., 2025a. Barrier option pricing and volatility surface predicting with an extended physics-informed neural network. *Expert Syst Appl*, 291:

128279. https://doi.org/10.1016/j.eswa.2025.128279

Chen Y, Lü X, Tian H, et al., 2025b. Physics-informed neural network for barrier option pricing in coupled financial quantitative system with varying interest rate and volatility. *Eng Anal Bound Elem*, 180:106457. https://doi.org/10.1016/j.enganabound.2025.106457

Guo LT, Zhang Y, Li Y, 2021. An intelligent electromagnetic environment reconstruction method based on super-resolution generative adversarial network. *Phys Commun*, 44:101253. https://doi.org/10.1016/j.phycom.2020.101253

Guo MH, Lü X, Jin YX, et al., 2025. Extraction and reconstruction of variable-coefficient governing equations using Res-KAN integrating sparse regression. *Phys D Nonl Phenom*, 481:134689. https://doi.org/10.1016/j.physd.2025.134689

IEC/IEEE, 2020. Measurement Procedure for the Assessment of Specific Absorption Rate of Human Exposure to Radio Frequency Fields from Hand-Held and Body-Mounted Wireless Communication Devices—Part 1528: Human Models, Instrumentation, and Procedures (Frequency Range of 4 MHz to 10 GHz). IEC/IEEE 62209-1528-2020. https://doi.org/10.1109/IEEESTD.2020.9231298

IEC/IEEE, 2022a. Assessment of Power Density of Human Exposure to Radio Frequency Fields from Wireless Devices in Close Proximity to the Head and Body (Frequency Range of 6 GHz to 300 GHz)—Part 1: Measurement Procedure. IEC/IEEE 63195-1-2022. https://doi.org/10.1109/IEEESTD.2022.9770427

IEC/IEEE, 2022b. Assessment of Power Density of Human Exposure to Radio Frequency Fields from Wireless Devices in Close Proximity to the Head and Body (Frequency Range of 6 GHz to 300 GHz)—Part 2: Computational Procedure. IEC/IEEE 63195-2-2022. https://doi.org/10.1109/IEEESTD.2022.9770556

Ledig C, Theis L, Huszár F, et al., 2017. Photo-realistic single image super-resolution using a generative adversarial network. Proc IEEE Conf on Computer Vision and Pattern Recognition, p.105-114. https://doi.org/10.1109/CVPR.2017.19

Lepcha DC, Goyal B, Dogra A, et al., 2023. Image super-resolution: a comprehensive review, recent trends, challenges and applications. *Inform Fus*, 91:230-260. https://doi.org/10.1016/j.inffus.2022.10.007

Li CS, Yang L, Lu BS, et al., 2016. A reverberation chamber for rodents' exposure to wideband radiofrequency electromagnetic fields with different small-scale fading distributions. *Electromagn Biol Med*, 35(1):30-39. https://doi.org/10.3109/15368378.2014.960086

Li K, Kodera S, Poljak D, et al., 2023. Calculated epithelial/absorbed power density for exposure from antennas at 10–90 GHz: intercomparison study using a planar skin model. *IEEE Access*, 11:7420-7435. https://doi.org/10.1109/ACCESS.2023.3238582

Li K, Kodera S, Poljak D, et al., 2024. Spatially averaged epithelial/absorbed power density for nonplanar skin models exposed to antenna at 10–90 GHz. *IEEE Access*, 12:15379-15389. https://doi.org/10.1109/ACCESS.2024.3358109

Lin JC, 2016. Human exposure to RF, microwave, and millimeter-wave electromagnetic radiation [health effects]. *IEEE Microw Mag*, 17(6):32-36. https://doi.org/10.1109/MMM.2016.2538540

Liu ZC, Allal D, Cox M, et al., 2020. Discrepancies of measured SAR between traditional and fast measuring systems. *Int J Environ Res Publ Health*, 17(6):2111. https://doi.org/10.3390/ijerph17062111

Ma C, Rao YM, Cheng YA, et al., 2020. Structure-preserving super resolution with gradient guidance. Proc IEEE Conf on Computer Vision and Pattern Recognition, p.7766-7775. https://doi.org/10.1109/CVPR42600.2020.00779

Mirza M, Osindero S, 2014. Conditional generative adversarial nets. https://arxiv.org/abs/1411.1784.

Qamar Z, Naeem U, Khan SA, et al., 2016. Mutual coupling reduction for high-performance densely packed patch antenna arrays on finite substrate. *IEEE Trans Antenn Propag*, 64(5):1653-1660. https://doi.org/10.1109/TAP.2016.2535540

Sharma P, Kumar M, Sharma HK, et al., 2024. Generative adversarial networks (GANs): introduction, taxonomy, variants, limitations, and applications. *Multim Tools Appl*, 83(41):88811-88858. https://doi.org/10.1007/s11042-024-18767-y

Su YB, Lue X, Li SK, et al., 2024. Self-adaptive equation embedded neural networks for traffic flow state estimation with sparse data. *Phys Fluids*, 36(10):104127. https://doi.org/10.1063/5.0230757

Sun J, Sun J, Xu ZB, et al., 2011. Gradient profile prior and its applications in image super-resolution and enhancement. *IEEE Trans Image Process*, 20(6):1529-1542. https://doi.org/10.1109/TIP.2010.2095871

Wang X, Sun LJ, Chehri A, et al., 2023. A review of GAN-based super-resolution reconstruction for optical remote sensing images. *Remote Sens*, 15(20):5062. https://doi.org/10.3390/rs15205062

Wang Z, Bovik AC, Sheikh HR, et al., 2004. Image quality assessment: from error visibility to structural similarity. *IEEE Trans Image Process*, 13(4):600-612. https://doi.org/10.1109/TIP.2003.819861

Wu TN, Hadjem A, Wong MF, et al., 2010. Whole-body new-born and young rats' exposure assessment in a reverberating chamber operating at 2.4 GHz. *Phys Med Biol*, 55(6):1619. https://doi.org/10.1088/0031-9155/55/6/006

Wu TN, Shao Q, Yang L, 2013. Simplified segmented human models for whole body and localised SAR evaluation of 20 MHz to 6 GHz electromagnetic field exposures. *Radiat Prot Dosim*, 153(3):266-272. https://doi.org/10.1093/rpd/ncs105

Wu TN, Chen YM, Li CS, 2024. Efficient evaluation of epithelial/absorbed power density by multiantenna user equipment with SAM head model. *IEEE Antenn Wirel Propag Lett*, 23(12):4059-4063. https://doi.org/10.1109/LAWP.2024.3421367

Xue WF, Zhang L, Mou XQ, et al., 2014. Gradient magnitude similarity deviation: a highly efficient perceptual image quality index. *IEEE Trans Image Process*, 23(2):684-695. https://doi.org/10.1109/TIP.2013.2293423

Yan H, Wang ZX, Xu ZJ, et al., 2024. Research on image super-resolution reconstruction mechanism based on convolutional neural network. Proc 4th Int Conf on Artificial Intelligence, Automation and High Performance Computing, p.142-146. https://doi.org/10.1145/3690931.3690956

Yang L, Zhang C, Chen ZY, et al., 2021. Functional and network analyses of human exposure to long-term evolution signal. *Environ Sci Pollut Res*, 28(5):5755-5773. https://doi.org/10.1007/s11356-020-10728-w

Yin YH, Lü X, Li SK, et al., 2025. Graph representation learning in the ITS: car-following informed spatiotemporal network for vehicle trajectory predictions. *IEEE Trans Intell Veh*, 10(4):2642-2652. https://doi.org/10.1109/TIV.2024.3381990